ELSEVIER

Contents lists available at ScienceDirect

Ceramics International

journal homepage: www.elsevier.com/locate/ceramint





Lanthanides disorder in tantalates and niobates perovskites: structure and electric properties

Théo Grivois ^{a,*} ^b, Tomas Šalkus ^b, Jiacheng Yu ^c, Vilma Kavaliukė ^b ^b, Pierre-Eymeric Janolin ^c ^b, Saulius Daugėla ^b, François Goutenoire ^a, Anthony Rousseau ^a, Maud Barre ^a ^b

- a Institut des Molécules et Matériaux du Mans (IMMM), UMR CNRS 6283, Le Mans Université, Avenue Olivier Messiaen, F-72085, LE MANS Cedex 9, France
- b Institute of Applied Electrodynamics and Telecommunications, Faculty of Physics, Vilnius University, Sauletekio 9-3, LT-10257, Vilnius, Lithuania
- ^c Université Paris-Saclay, CentraleSupélec, CNRS, Laboratoire SPMS, 8-10 rue Joliot Curie, 91990 Gif-sur-Yvette, France

ARTICLE INFO

Keywords:
Perovskite
Electrical properties
Electrostriction
Disorder symmetry
Distortion
Tantalates
Niobates

ABSTRACT

This study investigates the electrical properties of lanthanide perovskites with large lanthanide ions in partially occupied structures ($Ln_{1/3}BO_3$ with Ln=La, Ce, Pr, Nd, Gd and B=Ta or Nb) and correlates these properties with their structural and microstructural characteristics. The first comparative analysis of these properties across both tantalate and niobate families. Crystal structures were examined using electron diffraction and X-ray diffraction to identify framework distortions in the perovskite structure and the local environment of the lanthanide ions. High-resolution transmission electron microscopy (HRTEM) offered further insights into the spatial distribution of lanthanides within the structure. Complex impedance spectroscopy measurements on sintered pellets (with densities up to 90 %) indicated low ionic conductivity, suggesting that rare earth cations act as mobile charge carriers. Additionally, this study reports the first electrostriction measurements on these materials, revealing that the presence of numerous and disordered vacancies significantly reduces the electromechanical responses.

1. Introduction

Perovskites are among the most extensively studied structures due to their wide range of possible chemical compositions $(A_x B_y X_{3-\delta})$ and properties, particularly in oxides (X = O). The ideal structure of this family is cubic ($Pm \overline{3} m [1]$), but numerous substructures and distortions have been reported [2-7]. The stability and flexibility of the octahedral framework enables various aliovalent and isovalent substitutions at both the *A* and *B* sites allowing the tuning of electrical [8–11], optical [12,13] and/or piezoelectric properties [14,15]. Among these formulations, the structural family with an incomplete cationic sublattice $Ln_{1/3}\square_{2/3}BO_3$ (where Ln = La, Ce, Pr, Nd or Gd and B = Ta or Nb) is particularly interesting. Although these materials were first investigated in the 1960's [16,17]. However, little attention has been given to the role of the local environment around large lanthanide cations [18] (e.g., La³⁺, Nd^{3+} , $r \approx 1.3$ Å) and its impact on their mobility within the lattice [19] despite the potential for the local or long-distance mobility of the lanthanides and their possible ordering can result in interesting properties of piezoelectricity, electrostriction, or even ionic conduction [20-23].

From a structural perspective, Ln^{3+} cations have been shown to exhibit A-site ordering, forming layered arrangements. This ordering results in a doubling of the unit cell along the c-axis, leading to different symmetries depending on the lanthanide ion. In tantalates (B= Ta), the structure is tetragonal for $Ln = La^{3+}$, Er^{3+} , Tm^{3+} and orthorhombic for $Ln = Ce^{3+}$, Pr^{3+} , Nd^{3+} [24]. The structure of $Gd_{1/3}TaO_3$ remains under debate, having been reported as either orthorhombic (*Cmmm*) [25] or tetragonal (*P4/mmm*) [24]. In niobates (B= Nb), the structures are orthorhombic but the doubling has been reported either only along the c axis (resulting in a *Pmmm* supercell) [26] or along all three axes (leading to a *Cmmm* space group) [27,28].

Although the electrical conductivity of these ceramics has been studied over a broad temperature range (from ambient to 1273 K), the nature of the charge carriers remains a topic of debate. Various conduction mechanisms have been reported for niobates, including ionic conduction (with rare-earth ions as charge carriers at room temperature [19,29]), electronic conduction [30], and protonic conduction [31]. In contrast, their electromechanical properties are more straightforward: piezoelectricity is forbidden by symmetry as all these perovskites

E-mail address: Theo.Grivois@univ-lemans.fr (T. Grivois).

^{*} Corresponding author.

crystallize in centrosymmetric space groups. Therefore, these materials can only exhibit electrostriction.

The objective of this study is to determine the nature of the charge carriers in niobate and tantalate perovskite oxides with an incomplete lanthanide sublattice $Ln_{1/3}\square_{2/3}BO_3$ (where Ln=La, Ce, Pr, Nd, or Gd and B=Ta or Nb) and to establish the influence of the local environment of lanthanide (coordination, polyhedral distortion, and tilting) or distribution on their electrical properties. Following synthesis via a solid-state route, the crystalized phases of the powders were characterized by X-ray diffraction. The incomplete cationic sub-lattice was studied using transmission electronic microscopy in both diffraction and HRTEM modes. Several electrical measurements were then performed on sintered pellets to study the conductivity, permittivity, polarizability, and strain under electric field of sintered pellets were then investigated over the 30–800 K temperature range.

2. Experimental section

Synthesis: Polycrystalline samples of $Ln_{1/3}{\rm NbO_3}$ and $Ln_{0.33}{\rm TaO_3}$ (where Ln = La, Ce, Pr, Nd and Gd) were prepared by solid-state reaction. Powders of $Ln_2{\rm O_3}$ with Ln = La, Ce, Nd, and Gd, Pr₆O₁₁ (Alpha Aesar 99.99 %) were preheated at 1000 °C for one night. These powders were then ground in an agate mortar with Ta₂O₅ (Thermo Scientific 99.5 %) or Nb₂O₅ (Thermo Scientific 99.5 %). The obtained mixture was placed in alumina crucibles and heated for 12h between 1100 °C and 1600 °C depending on the composition (see Table 1). Elemental analysis in SEM (EDX) of the samples showed no alumina pollution from the crucibles. The powders were compacted into 10 mm-diameter pellets under a uniaxial pressure of 2500 bars and then sintered for 2h at specific sintering temperatures (higher than their synthesis temperature; see Table 1).

X-ray powder diffraction patterns were collected on a PANalytical Empyrean diffractometer with a Bragg Brentano reflection montage, equipped with a copper anticathode and a PIXEL fast detector. The measurements were recorded with a 0.007° step and an acquisition time of 200s (per step) between 5° and 125° in 20. Phase identifications were conducted using the software Highscore Plus [32]. The diffraction data were analyzed using the Rietveld method implemented in the Jana 2020 program [33].

The TEM experiments were realized with a TEM JEOL JEM 2100 HR (LaB $_6$ filament) operating at 200 kV and equipped with a side entry \pm 30° double tilt sample holder. The Selected Area Electron Diffraction (SAED) method (parallel beam) was performed with a length of camera fixed at 100 cm and the patterns were recorded by a camera CCD ORIUS 200 D. An EDX JEOL SM-JED2300T-30 $\,\mathrm{mm}^2$ detector was used for elemental analysis. In the case of high-resolution images (HRTEM), we used ULTRA SCAN (USC) 1000 XP. For the preparation of the sample, the powder was dispersed in ethanol and one drop of this suspension was deposited on a copper grid (300 mesh).

The grain size was determined by scanning electron microscopy (SEM). Microstructural observations and elemental analysis were performed using a microscope JEOL JSM 6510-LV coupled to an EDX detector (Oxford Xmax - 20 $\,\text{mm}^2$) with an accelerating voltage of 20 kV; the value of spot size was 35. The samples were sintered pellets, polished first with a silicon carbide disc (with the grain size around 18 $\,\mu\text{m}$) and then with a diamond gel (with the size of 1 $\,\mu\text{m}$). To reveal the grain boundaries, the ceramics underwent a thermal etching treatment for 2 h at 50 $^{\circ}\text{C}$ below their respective sintering temperatures.

Impedance spectroscopy measurements were performed on a custom

impedance spectrometer [34]. The equipment operates by vector voltmeter – amperemeter method and is based on TiePie Handyscope HS3 computer oscilloscope, which has a built-in functional generator and two channels for signal measurements. The temperature was measured by an Amprobe TMD90A digital thermometer.

The measurements were carried out in air; the temperature changed from 300 to 800 K while heating and cooling the sample at 2 deg/min, and the temperature was stabilized for at least 2 min before each measurement. The frequency range was from 2 MHz down to 10 Hz. The measurement equipment [34] allowed us to use small samples, cylindrical, with diameters up to 3 mm and about 1 mm in thickness. Platinum paste (71 % Pt, MaTeck GmbH) was applied on both faces of the cylinder, dried for 1 h at 400 $^{\circ}\text{C}$, and finally annealed at 700 $^{\circ}\text{C}$ for 20 min to form the conductive electrodes. The ZView software was used for data analysis by fitting equivalent circuit model parameters to the experimental data. In addition, the 4-electrode impedance measurement method was employed to better assess the influence of the electrode-ceramic interfaces on the impedance spectra.

The polarization and longitudinal displacement for electrostriction measurements were carried out in the AixACCT Measurement System (Piezo Measurement Module) at 100 Hz and room temperature. Possible quadratic deformations (electrostatic displacement and Maxwell strain) were excluded using of standard samples: 0.9 Pb(Mg1/3Nb2/3)O3-0.1PbTiO3 (PMN-10PT) (positive quadratic strain under the electric field) and glass (no measurable response) under the same conditions. The precision of the interferometer (due to the ambient mechanical noise) is below 1 nm by averaging 10 times the measurements, corresponding to a 10^{-6} strain for ceramics with a typical thickness of 1 mm. The relative permittivity and electrostrictive coefficients were extracted through sinusoidal fitting of the time-dependent polarization and strain signals measured simultaneously.

3. Results and discussion

3.1. Crystal structure

X-ray Diffraction The X-ray diffraction data for $La_{1/3}TaO_3$ confirm the P4/mmm tetragonal space group [24,25] (see Fig. 1) with the cell parameters a=3.916(1) Å and c=7.909(3) Å.

The TaO $_6$ octahedra are regular and unrotated, corresponding to the Glazer notation $a^0\ b^0\ c^0\ [35]$. In this structure, the cuboctahedron in perovskite is almost regular with La-O distances between 2.732(2) Å and 2.769(2) Å. The diagonals of the square/rhombus faces shared by two successive cuboctahedra are 3.916(2) Å and 4.100(2) Å (an example of these distances is shown in Fig. 2).

Inaguma et al. reported such distances around 4 Å in their investigations of conducting pathways in lanthanide perovskites [36]. These values are crucial to the possible lanthanum mobility in such a structure, as they represent the bottleneck ${\rm La}^{3+}$ cations will have to go through to jump from one site to another.

All other tantalates and niobates crystallize in the orthorhombic space group *Cmmm* with a $\approx b \approx c \approx 2a_{perovskite}$, in agreement with previous reports [25,27,37,and38]], including for $Gd_{1/3}TaO_3$ (in agreement with Ref. [25] and contrary to Ref. [24]). It is common for lanthanum to exhibit behaviour different from that of the other lanthanides, especially in compounds where the cation does not have a mixed valence state. This is indeed observed in NASICON-type compounds, where $La_{1/3}Ti_2(PO_4)_3$ crystallizes in the space group R-3 [39], which is common for this structural family, whereas $La_{1/3}Zr_2(PO_4)_3$

Table 1Temperatures of perovskites' synthesis and ceramics sintering.

	$La_{1/3}TaO_3$	$La_{1/3}NbO_3$	$Nd_{1/3}TaO_3$	$Nd_{1/3}NbO_3$	$Pr_{1/3}TaO_3$	$Pr_{1/3}NbO_3$	$Gd_{1/3}TaO_3$	$Ce_{1/3}NbO_3$	Ce _{1/3} TaO ₃
T _{synthesis}	1400 °C	1200 °C	1350 °C	1250 °C	1400 °C	1250 °C	1450 °C	1200 °C	1400 °C
T _{sintering}	1500 °C	1300 °C	1550 °C	1400 °C	1550 °C	1350 °C	1600 °C	1275 °C	1600 °C

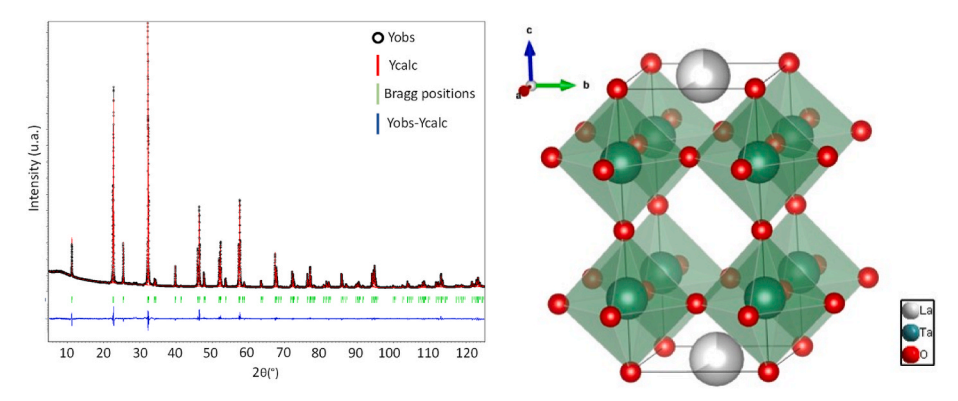


Fig. 1. Refined X-ray diffraction diagram confirming the P4/mmm space group and corresponding structure projection of La_{0.33}TaO₃.

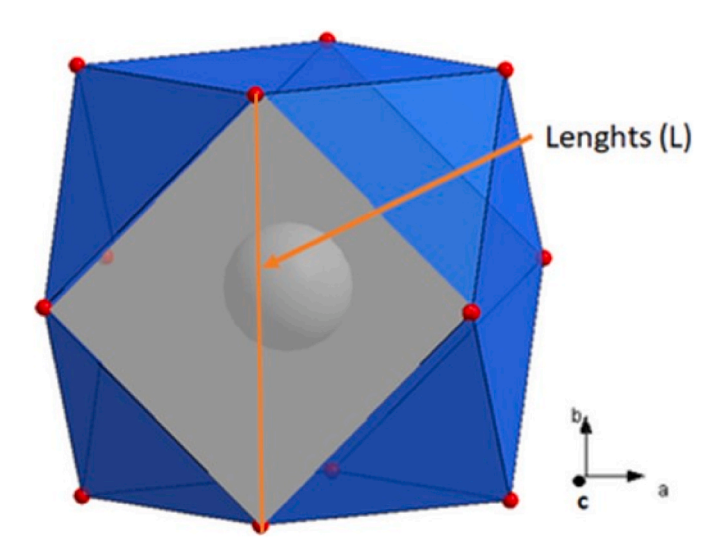


Fig. 2. Representation of the cuboctahedra with the edges around the lanthanum atom. The distortion of the cuboctahedra changes the energy barrier to be overcome for the migration of a lanthanide ion between nearest-neighbor sites.

crystallizes in the space group *P*-3 [40]. Moreover, it is also frequently observed that tantalum and niobium show different behaviour within the same structure type—for example, in Ruddlesden-Popper phases (Sr₂Nb₂O₇ crystallizes in the orthorhombic space group *Cmc*2₁ [41], while Sr₂Ta₂O₇ crystallizes in the orthorhombic space group *Cmcm* [2]) or, as in our case here, in perovskites (KNbO₃ has an orthorhombic cell with space group *Amm*2, whereas KTaO₃ has a cubic cell with space group *Pm*-3*m* [42]). Even if it is not clear in the literature, one may suggest that such a specific behaviour is due to the combination of polarizability of lanthanum ions and the non-reducibility of tantalum ions Ta⁵⁺ which prevents any local electronic defects that could favour a certain flexibility of the structural skeleton. The results from Rietveld refinements of the X-ray data for all compounds (structural parameters,

R-reliability factors) are presented in Table 2 and the Rietveld plots are in S1 to S4.

The unit cell volume decreases with the due to the decreasing ionic radius of the rare earth (from 1.36 Å to 1.20 Å for La³⁺ and Gd³⁺, respectively) in the perovskite structure. Since B cations are of similar size ($r_{Ta} = r_{Nb} = 0.64 \text{ Å}$), the cell volume of tantalates is similar to the ones of their niobates counterparts. The orthorhombic symmetry observed in these materials is somewhat unexpected when considering the Goldschmidt tolerance factor t (with t=($r_{Ln} + r_O$)/($\sqrt{2(r_B + r_O)}$, where r_{Lp} , r_{B} and r_{O} are the ionic radii of the rare earth, the B cation and the atom of oxygen, respectively) even if the evolution of this factor is consistent with the evolution of ionic radius of lanthanide. Indeed, even if we note a logical decrease of the t values with the ionic radius of the lanthanide (for $r_{La} = 1.36$ Å, t = 0.97 and $r_{Gd} = 1.20$ Å, t = 0.91) all of these values remain in the domain between 0.9 and 1 which should correspond to the undistorted cubic cell, whereas an orthorhombic (tetragonal) distortion are consistent with smaller (larger) t values. Nevertheless, X-ray diffraction refinements unambiguously show that these materials are not monophasic cubic samples. In the Cmmm space group the perovskite A site is split over two crystallographic sites 4g (\approx 0.25 0 0) and 4h (\approx 0.25 0 ½). Refinement of the site occupancies leads to one site totally empty (4h) and the 4g one occupied with a twothirds occupancy. This confirms the results obtained by Kepaptsoglou et al. [37] for La_{0.33}NbO₃. For these perovskites, the loss of symmetry (from cubic to orthorhombic) results from the A-site ordering, and then the doubling of the a and b cell parameters is due to the antiphase tilting of the TaO₆ or NbO₆ octahedra along the c-axis, as shown in Fig. 3. This structural evolution is consistent with the symmetry groups relationship model proposed by Howard ($Pm \ \overline{3} \ m \rightarrow P4/mmm \rightarrow Cmmm$) [43].

The rotation pattern of these octahedra is noted $a^ b^0$ c^0 [35]. The value of these octahedra (TaO_6 or NbO_6) tilt angle increases when the atomic radius of the rare earth decreases (from $\approx\!4^\circ$ for La_{1/3}NbO_3 -consistently with Ref. [38]- to $\approx 7^\circ$ for Nd_1/3NbO_3 and from 0° for La_{0.33}TaO_3 to $\approx 7^\circ$ for Gd_0.33TaO_3). The cuboctahedral cages are heavily distorted in all these perovskite structures. To evidence the distortion of these cuboctahedra, the lengths of the smallest and largest diagonals of rhombus faces are reported in Table 3 with the minimal and maximal

 Table 2

 Results of the Rietveld refinements for all the tantalates and niobates.

	$La_{1/3}TaO_3$	$La_{1/3}NbO_3$	$Nd_{1/3}TaO_3$	$Nd_{1/3}NbO_3$	$Pr_{1/3}TaO_3$	$Pr_{1/3}NbO_3$	$Gd_{1/3}TaO_3$	$Ce_{1/3}NbO_3$	Ce _{1/3} TaO ₃
Space group	P4/m m m	C m m m	C m m m	C m m m	C m m m	C m m m	C m m m	C m m m	C m m m
Z	2	8	8	8	8	8	8	8	8
a (Å)	3.91599(1)	7.83176(4)	7.81024(3)	7.81159(5)	7.81510(4)	7.8168(5)	7.72918(5)	7.82217(4)	7.82318(3)
b (Å)	3.91599(1)	7.81265(4)	7.76268(3)	7.75966(4)	7.77704(4)	7.77002(5)	7.73533(5)	7.78352(4)	7.80166(3)
c (Å)	7.90892(3)	7.90527(4)	7.82487(3)	7.83385(5)	7.84502(4)	7.84706(6)	7.78542(4)	7.86936(5)	7.87479(3)
Volume (Å ³)	121.283(5)	483.697(5)	474.410(4)	474.852(6)	476.808(5)	476.607(6)	465.473(5)	479.118(5)	480.629(4)
V/Z (Å ³)	60.641(3)	60.462(3)	59.301(2)	59.356(3)	59.601(3)	59.576(3)	58.184(2)	59.890(3)	60.078(2)
R _{Bragg} (%)	2.31	4.69	2.19	5.25	3.73	5.65	4.23	4.42	2.35

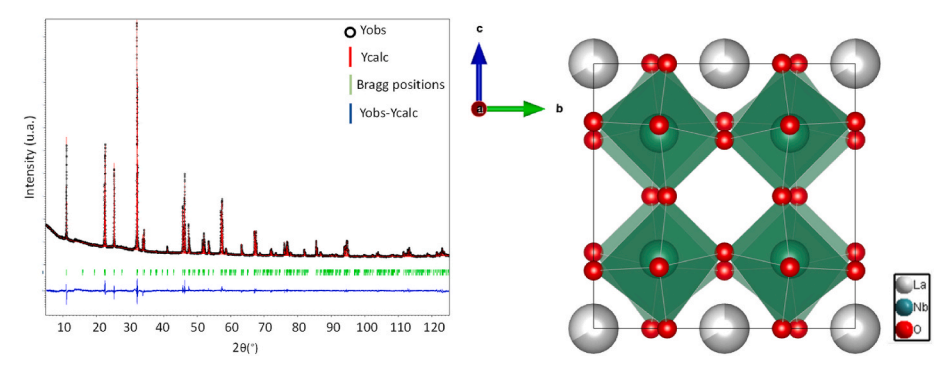


Fig. 3. Refined X-ray diffraction diagram confirming the Cmmm space group and structure projection along [100] for La_{0.33}NbO₃ which confirm the Glazer notation a⁻ b⁰ c⁰.

Table 3 – Characteristic distances and lengths of the rhombus of cuboctahedron illustrating the distortion of the cuboctahedra cages in $Ln_{1/3}BO_3$.

Formula	Ln-O _{min} (Å)	Ln-O _{max} (Å)	L _{min} (Å)	L _{max} (Å)
La _{1/3} TaO ₃	2.732(2)	2.769(2)	3.916(2)	4.100(2)
$La_{1/3}NbO_3$	2.575(6)	2.980(6)	3.425(6)	4.553(6)
$Pr_{1/3}TaO_3$	2.490(7)	3.043(7)	3.165(7)	4.723(7)
$Pr_{1/3}NbO_3$	2.537(6)	2.950(7)	3.311(7)	4.458(7)
$Nd_{1/3}TaO_3$	2.507(6)	3.013(7)	3.150(7)	4.513(7)
$Nd_{1/3}NbO_3$	2.476(5)	3.047(6)	3.140(6)	4.592(6)
$Gd_{1/3}TaO_3$	2.42(2)	3.025(9)	2.944(1)	3.100(1)

distances Ln-O.

For most of the compositions we observe highly distorted rhombus faces with a large difference between the small and large diagonals. Knowing that these rhombus faces represent the bottleneck through which lanthanides may jump, we can suppose that thermal agitation allows a flexibility of this face, arranging a pathway for cations. From this hypothesis, it is important to note that $Gd_{1/3}TaO_3$ is the only

compound to present a rhombus face with two small diagonals that will prevent any atom from going through, even supposing thermal agitation and flexibility. From this result, we expect a lower mobility of Gd^{3+} in perovskite in comparison with other lanthanides.

Electron Microscopy. Two samples (La_{1/3}TaO₃ and La_{1/3}NbO₃) were characterized by the SAED method in TEM to confirm the X-ray diffraction results. For La_{1/3}TaO₃, a STEM-EDX and a complete microstructural analysis were also performed with a framework reconstruction in the reciprocal space. The X map are shown in Supporting Information (Fig. S5) and the results of the reconstruction are presented in Fig. 4, the indexation of each image can be found in Figs. S6-S8. The STEM-EDX analysis shows a homogeneous chemical composition for all grains and the expected stoichiometric ratios of the 2 cations (La/Ta (experimental) = 0.32; La/Ta(stoichiometric) = 0.33). On the reconstruction (Fig. 4) the zone axis of the main picture is [001]. For this compound (La_{1/3}TaO₃), all the reflections are indexed with the extinction symbol *P* - - - which is consistent with a tetragonal cell in the space group P4/mmm. Furthermore, the parameters obtained in microscopy agree with the X-ray diffraction ones (3.93(2) Å against 3.92(1) Å and 8.05(2) Å against 7.91(3) Å for TEM and X-ray diffraction respectively)

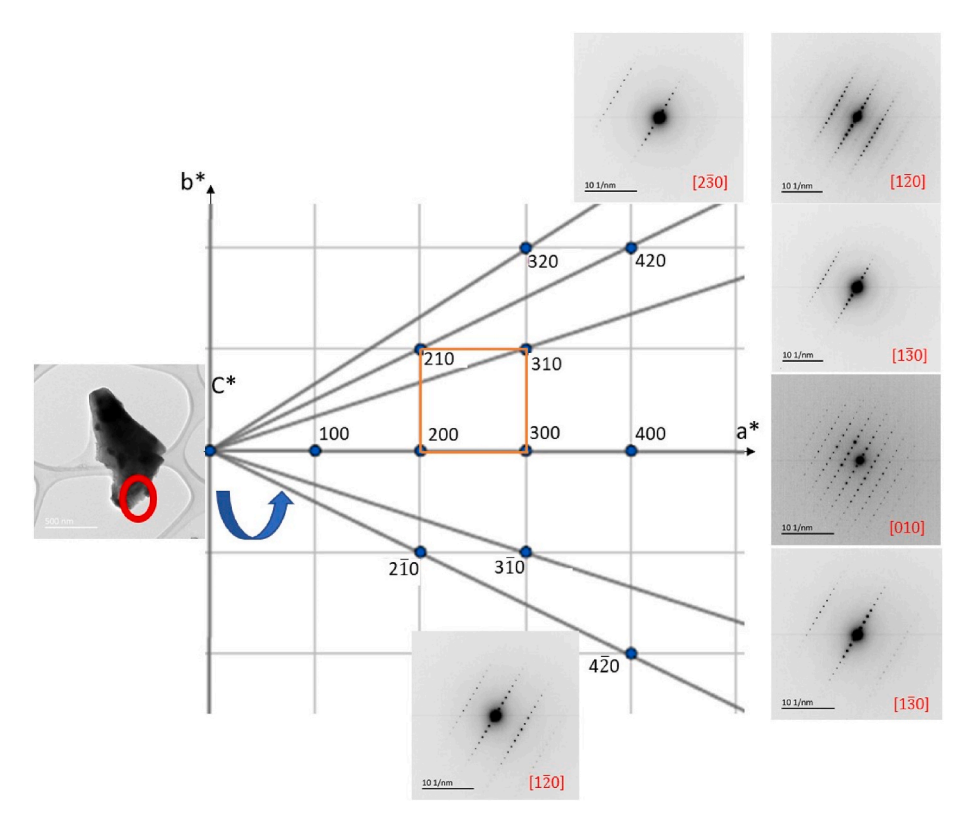


Fig. 4. Reconstruction of the $La_{0.33}TaO_3$ perovskite cell around the [001] axis in the reciprocal space which is consistent with the space group P4/mmm.

and the literature [25].

Furthermore, a high-resolution microstructural (HRTEM) study was undertaken on this compound to highlight the A-site vacancy distribution. The results, obtained with the zone axis $[1 \overline{1} 0]$, are shown in Fig. 5. The Fourier transform, as well as the image, indicates well-defined and crystallized grains. Its indexation is consistent with the space group P4/ mmm (Fig. 5a). In Fig. 5a, the [110] atomic plane is clearly defined and aligned along the c-axis. The atomic arrangement is consistent with the representation of the structure projection perpendicular to the zone axis $[1 \ \overline{1} \ 0]$ (Fig. 5b) with tantalum atoms aligned along the c-axis. The variation of profile line along the chosen atom row (red color line on Fig. 5a) is shown in Fig. 5c. The periodicity is respected and the experimental distance between two atoms (d_{Ta-Ta}) is about 3.7 Å. This distance corresponds to the distances between two tantalum atoms within the structure (3.9 Å, as determined by XRD). In our case, we observe some non-periodic variations of the intensity maxima. This variation corresponds to a variation of atomic density (as only Ta atoms occupy this column), which can only be explained by the absence or presence of lanthanum near the tantalum environment. Therefore, the distribution of lanthanum among the 1c site of the tetragonal cell (P4/

The same study was performed for the La $_{1/3}$ NbO $_3$ perovskite. The STEM EDX analysis showed a homogeneous distribution and the expected stoichiometric proportions of the two cations (La/Nb(experimental) = 0.32; La/Nb(stoichiometric) = 0.33; the X map are presented in Fig. S9). The picture in Fig. 6 shows an oriented base plane. Its zone axis appears to be [010]. Indeed, this indexation with the software CrysTbox [44], using the space group *Cmmm*, gives a higher rating and minimum total angular distance for this zone axis ([010]) than with other base planes. All the spots are indexed, confirming the orthorhombic rather than tetragonal symmetry of La $_{1/3}$ NbO $_3$, confirming the results of Ref. [37]. The cell parameters are also consistent with the ones obtained by X-ray diffraction (a = 7.96(2) Å against 7.83(4) Å and c = 8.04(1) Å against 7.90(3) Å).

This picture confirmed the systematic extinction symbol C — with h+1=2n for reflections h0l, h=2n for h00, and h=2n for 00l. These observations for the compound $La_{1/3}NbO_3$ are consistent with all the

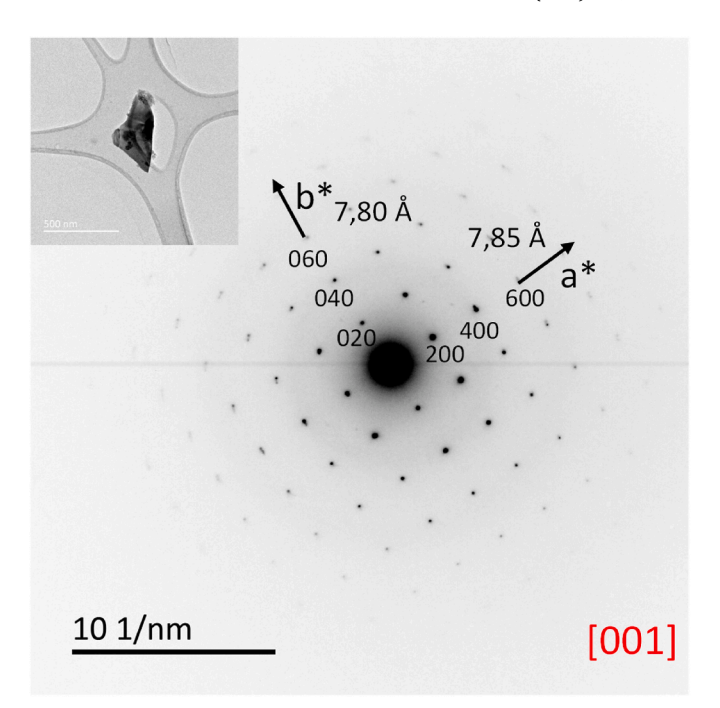


Fig. 6. Oriented picture with zone axis [001] for the compound $La_{1/3}NbO_3$ confirming the orthorhombic symmetry determined by X-ray diffraction.

ones made on $Nd_{1/3}NbO_3$ [45], corroborating the orthorhombic super-structure and definitively discarding tetragonal superstructure [26].

The high-resolution images obtained on this phase are summarized in Fig. 7. In Fig. 7a, the image and the Fourier transform exhibit very sharp spots underlying the high crystallinity and the right orientation of the grain. The indexation of the Fourier transform is consistent with the *Cmmm* space group and the zone axis for this picture is [001]. The corresponding representation of the structure is shown in Fig. 7b. Fig. 7c shows the variation of the profile line along the chosen atom row (light-

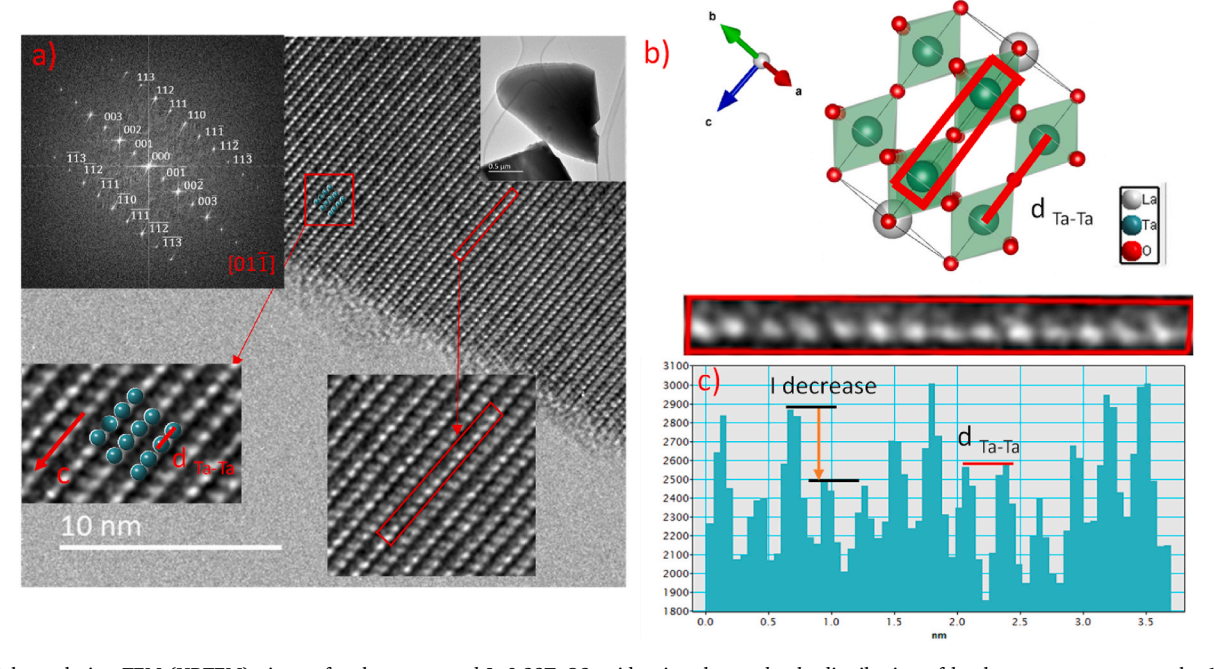


Fig. 5. High resolution TEM (HRTEM) picture for the compound La0.33TaO3 evidencing the randomly distribution of lanthanum atoms among the 1c site (a); representation of the crystal structure (b); FFT with the orientation of the crystal and HRTEM picture showing the intensity evolution for an atom row (defined by red rectangle in figure a) indicative of a random distribution of lanthanum atoms on the 1c site of the unit cell (c). (For interpretation of the references to color in this figure legend, the reader is referred to the Web version of this article.)

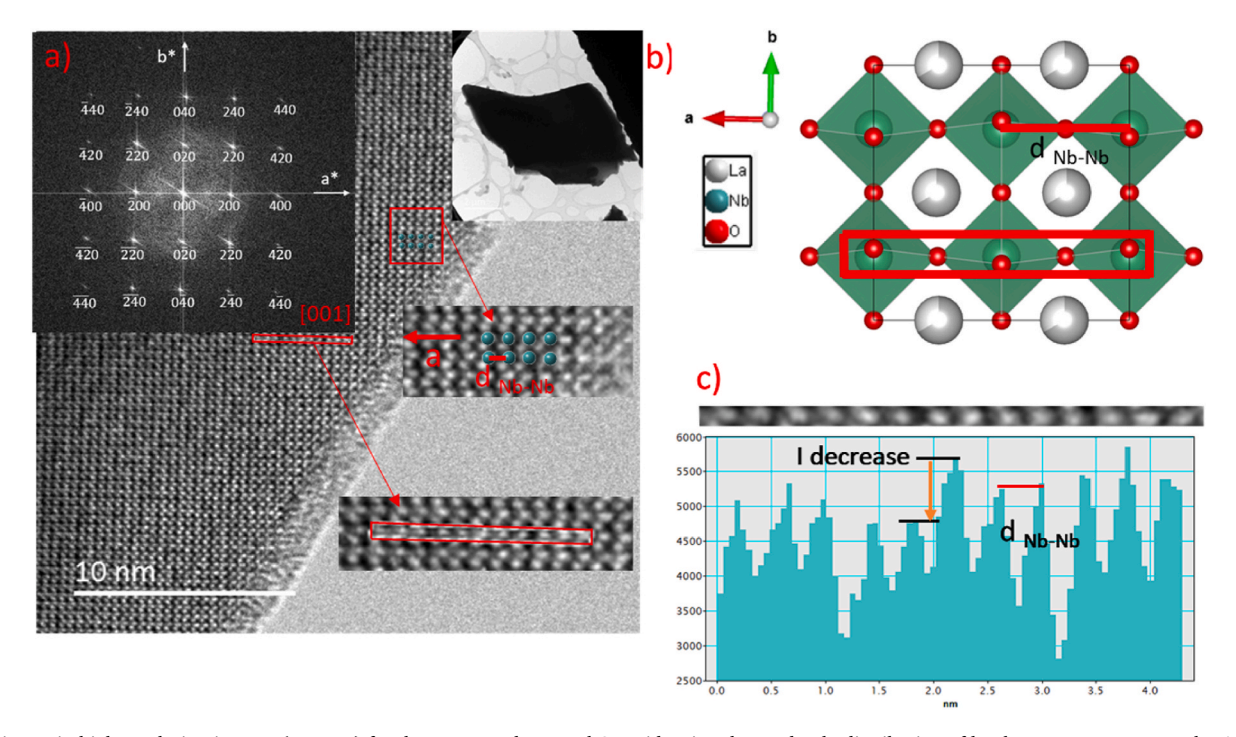


Fig. 7. Picture in high resolution in TEM (HRTEM) for the compound $La_{0.33}NbO_3$ evidencing the randomly distribution of lanthanum atoms among the 4g site (a); representation of the structure in this crystal (b); FFT with the orientation of the crystal and the picture in HRTEM and evolution of the intensity for an atom row (in red in figure a) (c). This shows the randomly distribution of lanthanum atoms among the 4g site. (For interpretation of the references to color in this figure legend, the reader is referred to the Web version of this article.)

colored dotted line in Fig. 7a). The periodicity between two consecutive intensity maxima corresponds to the cation-cation distance of 3.8 Å (d $_{\mbox{Nb-Nb}}$), consistent with the distance measured by XRD (around 3.9 Å). An HRTEM simulation of this compound along the [001] zone axis was performed (in Fig. S10). The simulated image is consistent with the experimental results, supporting and validating the previous observations. As for La $_{1/3}$ TaO $_{\mbox{3}}$, the maximum intensity values exhibit nonperiodic variations, leading to the same conclusion as for the previously discussed perovskite: the lanthanum atoms are randomly distributed among the 4g site of the orthorhombic cell (*Cmmm*).

3.2. Microstructure

A microstructural analysis by scanning electron microscopy (SEM) confirmed that the ceramics are well-sintered (see Fig. 8 for examples on cerium/praseodymium tantalates and niobates). This is consistent with relative densities greater than 90 % obtained in each case. The relative densities have been determined by calculating density ratios, the theoretical density was calculated using: $\rho_{theo} = Z^*M/(N^*V)$ where Z is the number of compound by cell, M is the molar mass (g/mol) of the compound, N is Avogadro's number (mol $^{-1}$) and V is the unit cell volume

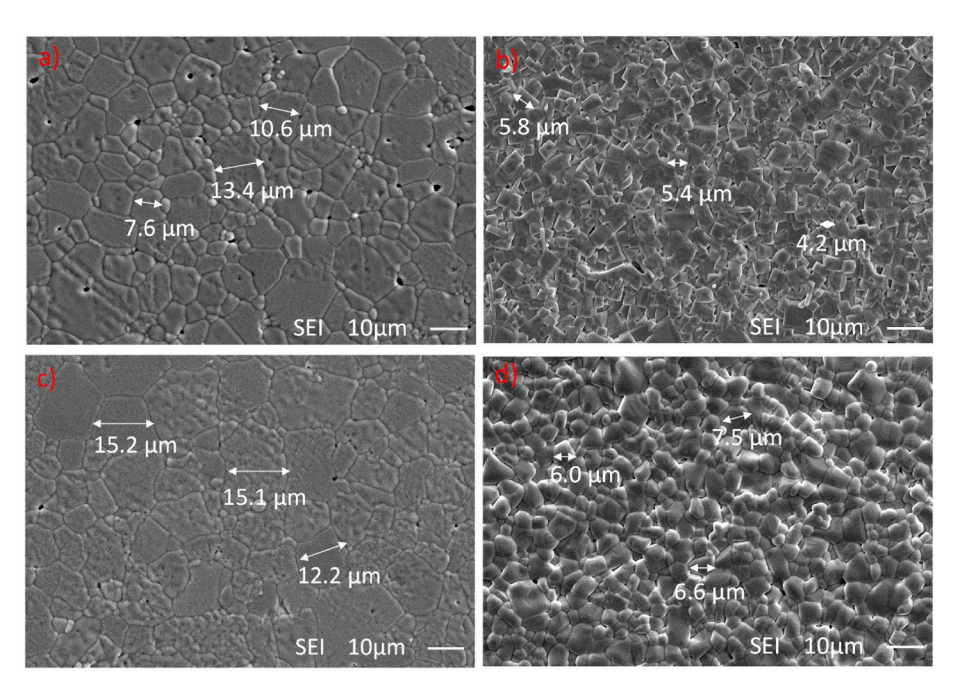


Fig. 8. SEM images confirming the well-sintered nature of the $Ce_{0.33}NbO_3$ (a), $Ce_{0.33}TaO_3$ (b), $Pr_{0.33}NbO_3$ (c) and $Pr_{0.33}TaO_3$ (d) ceramics.

(cm³). The experimental density was calculated using the formula $\rho_{exp}=m/(t^*r^{2*}\pi)$ where m is the mass of the pellet (g), t is the thickness of the pellet (cm) and r is the radius of the pellet (cm). Then the relative density (or compacity) of the pellet is: τ (%) $=100^*\rho_{exp}/\rho_{theo}.$

The grain sizes are all micrometric and appear logical, considering the synthesis and sintering temperatures. For nearly every composition the grain size distribution is homogeneous, and niobates present a larger grain size than tantalates (for example, in Fig. 8, around 14 μm and 10 μm for respectively $Pr_{1/3}NbO_3$ and $Ce_{1/3}NbO_3$ against 7 μm and 5 μm for $Pr_{1/3}TaO_3$ and $Ce_{1/3}TaO_3$). There are also differences in grain morphologies, indicative of a better sintering process in niobates (with welding and matter diffusion in grain boundaries and then grain growth) than in tantalates, where only good welding is present. Furthermore, an elemental analysis was carried out on each of these ceramics (S11 to S19), enabling us to verify that nominal and theoretical compositions match. For samples containing niobium, EDS elemental analysis shows slight surface inhomogeneity on the pellets, attributed to the presence of few rare-earth oxides. For example, the presence of Nd-rich grains observed in the EDS of Fig. S18 (corresponding to the Nd_{1/3}NbO₃

compound) can be explained by residual Nd_2O_3 impurities, which were also confirmed by the Rietveld refinement of the XRD data (see Fig. S3). The presence of this starting oxide indicates that the compound did not fully react in stoichiometric proportions with niobium oxide and was therefore present in a slight excess.

For the samples containing tantalum all the pellets are homogeneous.

3.3. Electrical properties

Impedance Spectroscopy. The impedance spectra of La_{1/3}NbO₃ ceramics measured at different temperatures are presented in Fig. 9. In all our graphs, we present electrical parameters which are normalized to the sample geometry; namely, we use specific complex resistivity ($\tilde{\rho} = \rho' - i\rho''$) in [$\Omega \bullet m$] units and conductivity σ in [S/m] units. The impedance spectrum measured at 300 K exhibits mainly one semicircle, followed by an increase in the imaginary impedance part at the lowest frequencies. Such a spectrum can be modelled with a simple equivalent circuit, as shown in Fig. 9 (d). The circuit consists of a resistance R_b and a constant phase element CPE_b in parallel, (which are associated with the

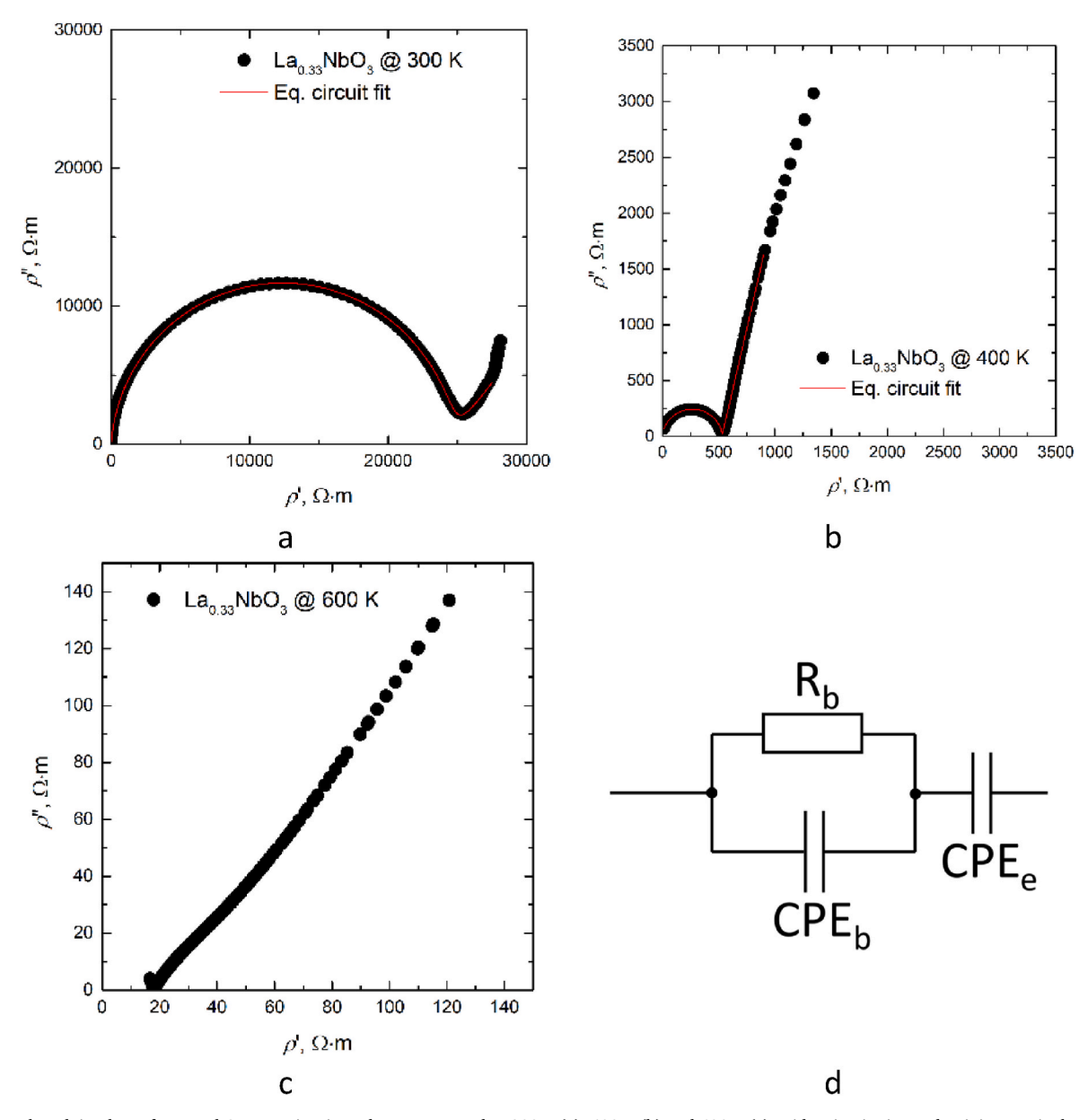


Fig. 9. Complex plain plots of La_{0.33}NbO₃ ceramics' impedance measured at 300 K (a), 400 K (b) and 600 K (c) evidencing ionic conductivity. Equivalent circuit (d) was used to fit experimental data. Note the frequency, even though not indicated, increases from the right to the left.

charge carriers' relaxation in the bulk of ceramics), and a constant phase element CPEe, which is associated with the capacitive behaviour of the ceramics and Pt electrode interface. The impedance of a CPE is $Z_{\text{CPE}} =$ $\frac{1}{(i\omega)^q Q}$, where $\omega = 2\pi f$ is the angular frequency, Q is the so-called pseudocapacitance and α is a constant related to the phase. The Q, α , and Rvalues were found from equivalent circuit fitting, and the true capacitances were calculated as $C = R^{\frac{1-\alpha}{\alpha}} \cdot Q^{\frac{1}{\alpha}}$. The obtained capacitance values are typical for the bulk of ceramics (C_b is in the range of 10^{-9} F/m) and solid electrolyte–metal electrode interface ($C_e \cong 10^{-5}$ F/m). At higher temperatures, the diameter of the semicircle (and the values of Rb) decreases. At the same time, the relaxation frequency shifts out of the measurement range, so only a small part of the semicircle is observed at 600 K. The lower-frequency-range capacitive part dominates the spectrum at the highest temperatures. The imaginary part of the resistivity increases to infinity with the decrease in frequency. Hence, the electrodes did not show any resistive behaviour. This observation provides insights about the charge carriers in these perovskites; firstly, the conductivity should be predominantly ionic, and if there were partial electronic or hole contribution to the conductivity, the imaginary part of impedance should become 0 at the lowest frequencies. Secondly, the oxygen ions are immobile as the electrode part of the impedance spectrum shows a totally ion-blocking character. Typically, in oxygen ion conductors, the spectrum part associated with the electrode shows one or several semicircles [46,47].

Very similar impedance spectra were obtained for the investigated ceramics with La, Nd, and Pr. Some more examples are shown in Fig. S20 (a - Nd $_{1/3}$ NbO $_3$, b - Nd $_{1/3}$ TaO $_3$, c- Pr $_{1/3}$ NbO $_3$, d- Pr $_{1/3}$ TaO $_3$). In all cases, the spectra consist of one semicircle, attributed to the bulk relaxation of charge carriers in ceramics, and one "spike," which represents the capacitive behaviour of the ceramic-metal electrode interface.

The absence of the second semicircle, usually observed in the spectra of ceramics and associated with ion transport across grain boundaries, is somewhat surprising. The rather inexpressive second semicircle can be seen for La_{1/3}TaO₃ ceramics (Figure S21 a). The equivalent circuit fitting showed that this semicircle could be due to grain boundary contribution ($C_2 = 7 \cdot 10^{-8}$ F/m, Figure S21 b). However, the four-electrode measurement clearly shows only one relaxation (Figure S21 c). Thus, as the measurement by the four-electrode method neglects all the processes taking place in the vicinity of the electrode, the above-mentioned second semicircle appears because of the relaxation process at the electrodeceramic interfaces. Then, the fact that grain boundaries do not play any role in the ion mobility results from the excellent microstructure of the ceramics. Hence, the ions do not encounter any resistance when moving from one grain to another.

Measurements were performed under dry air, with an initial heating step followed by cooling, to ensure that no residual humidity remained. Besides, the measured spectra do not change whether they were obtained during the heating or cooling stages. This shows that the potentially remaining air humidity does not affect the electrical properties of the ceramics. Thus, a protonic contribution to the conductivity is very unlikely.

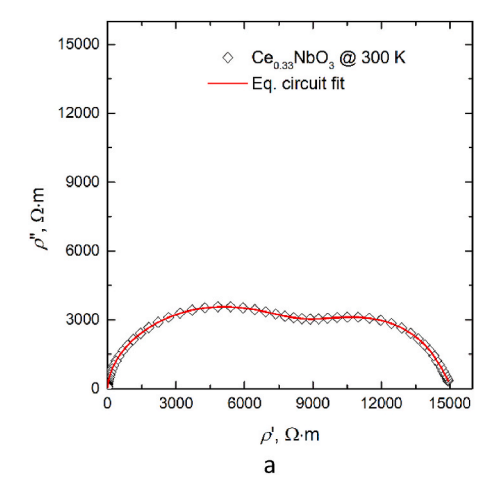
The impedance spectra of the perovskites with cerium and gadolinium differ from those described above. The spectra of $Ce_{1/3}NbO_3$, $Ce_{1/3}TaO_3$, and $Gd_{1/3}TaO_3$ ceramics at selected temperatures are presented in Fig. 10 and Fig. S22. The capacity of the second process (the one at lower frequency) in the sample $Ce_{1/3}NbO_3$ is 4×10^{-7} F/m. The first obvious feature is the absence of a capacitive-type part in the lower frequency range, which suggests that the electronic conductivity is significant in these materials.

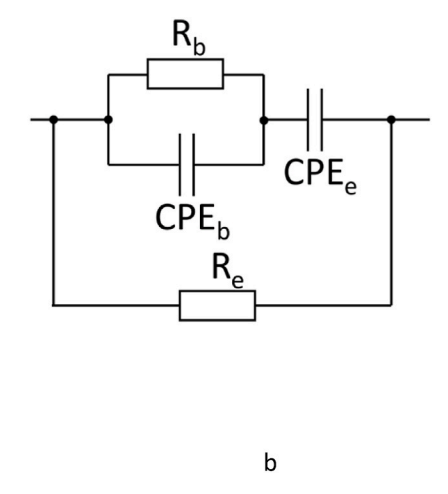
Therefore, an extra resistance element R_e is added in parallel to the equivalent circuit (see Fig. 10 b) in addition to the mobile ion contribution. In this model, R_e is the ceramics' electronic conductivity counterpart. Besides, its values are very close to the total conductivity. In this case, the ionic conductivity contribution cannot be seen directly from the impedance complex plane plots, and it can only be calculated from fitting parameters.

The conductivity values of the ceramics were calculated from the equivalent circuit fitting results: $\sigma_{\text{bulk,e}} = \frac{1}{R_*}$.

The temperature evolution of the bulk conductivity is presented in Fig. 11. By keeping the same cation on the perovskite B site, among pure ion conductors, it is observed that the ionic radius of the rare-earth element influences the conductivity values of all the ceramics: the larger the lanthanide ionic radius, the higher the ceramic's conductivity (with the exception of the cerium-containing composition, which also exhibits electronic conductivity). This trend can be explained by the distortions of the octahedra characteristic of perovskite structures. Indeed, as mentioned in the first part of this article, a larger rare-earth ionic radius leads to reduced lattice distortion, thereby facilitating the movement of charge carriers within the structure. This observation is consistent with results reported for fluorite-type CeO2 compositions doped with rare-earth elements, where the least distorted ceramics also showed the highest conductivity [48]. In our case lanthanum-containing perovskites are the most conductive, neodymium and praseodymium tantalates are almost identical in terms of conductivity, and neodymium niobate is much more conductive than praseodymium niobate. The conductivity does not strictly follow Arrhenius law ($\sigma_{
m bulk} \cdot T =$ $\sigma_0 \exp \frac{-\Delta E}{k_B T}$) over the whole temperature range. A change of slope requires the activation energies of bulk conductivity to be determined over two temperature ranges: 300-600 K and 600-800 K.

The ionic and electronic components of the conductivities of mixed





 $\textbf{Fig. 10.} \ \ \textbf{Impedance spectra of $Ce_{0.33}$NbO}_3 \ \ \textbf{measured at 300 K (a); equivalent circuit, which models both ionic and electronic conductivities (b).}$

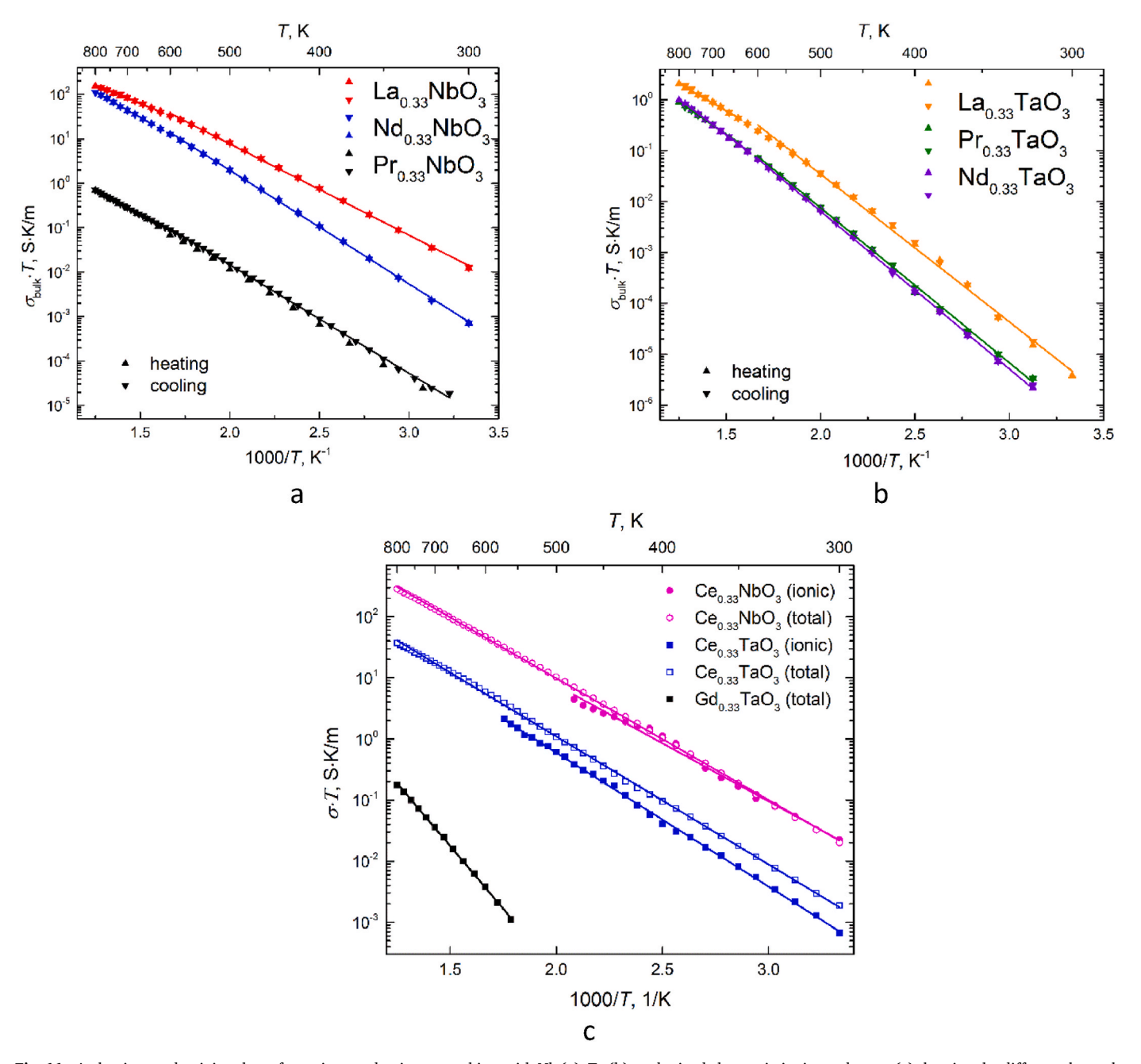


Fig. 11. Arrhenius conductivity plots of pure ion conducting perovskites with Nb (a); Ta (b); and mixed electronic-ionic conductors (c) showing the different thermal behaviour of ionic and electronic conductivities.

electronic-ionic conductors $Ce_{1/3}NbO_3$ and $Ce_{1/3}TaO_3$ are of comparable magnitudes, the ionic conductivity being slightly lower than the electronic one. Comparing the ionic conductivities of niobate perovskites, $La_{1/3}NbO_3$ and $Ce_{1/3}NbO_3$ have similar values at 300 K, when $Nd_{1/3}NbO_3$ is less conductive, while at higher temperatures (>500 K) $La_{1/3}NbO_3$ and $Nd_{1/3}NbO_3$ are better ionic conductors than $Ce_{1/3}NbO_3$. Among the tantalates, $Ce_{1/3}TaO_3$ shows the highest ionic conductivity. The charge carriers of $Gd_{1/3}TaO_3$ remain uncertain because of its low overall conductivity, the lowest among all the investigated perovskites, which may explain the absence of the electrode polarization phenomenon. Furthermore, $Gd_{1/3}TaO_3$ exhibits a strongly distorted local environment for Gd^{3+} cations with a very narrow bottleneck for ions to go through. This will be related to a higher activation energy and lowers conductivity values.

The dependence of the conductivities on the B-site ion for the same A-cation is shown in Fig. S23. In all cases, the niobates have higher

conductivities than tantalates. The difference is quite prominent (about two orders of magnitude) except for Pr-containing perovskites, but for the latter the conductivity values are low. This difference in conductivity between tantalates and niobates could be explained first by the better sintering process (resulting in a better microstructure) and then by the mixed valence of niobium. Indeed, this atom can easily be reduced by switching from Nb⁵⁺ to Nb⁴⁺, thus providing an electronic contribution to the observed conductivity values. Therefore, there could be local electronic exchanges within the structure.

The activation energies values presented in Table 4 show that the B-cation determines the barrier height for the ionic jumps. The conductivity activation energies of niobates are by ~ 0.1 eV lower than for tantalates, consistently with their higher conductivities.

The activation energies decrease at elevated temperatures for all pure-ion-conducting perovskites (La $_{1/3}$ NbO $_3$, La $_{1/3}$ TaO $_3$, Nd $_{1/3}$ NbO $_3$, Nd $_{1/3}$ TaO $_3$, Pr $_{1/3}$ NbO $_3$, Pr $_{1/3}$ TaO $_3$ and Gd $_{1/3}$ TaO $_3$). The difference is the

Table 4Activation energies of conductivity for the investigated perovskites.

	E _a 1, (eV) 300–600 K	E _a 2, (eV) 600–800 K		E _a 1, (eV) 300–600 K	E _a 2, (eV) 600–800 K
La _{1/3} NbO ₃	0.41	0.34	La _{1/3} TaO ₃	0.58	0.42
Nd _{1/3} NbO ₃	0.51	0.46	$Nd_{1/3}TaO_3$	0.62	0.56
Pr _{1/3} NbO ₃	0.49	0.44	$Pr_{1/3}TaO_3$	0.61	0.51
Ce _{1/3} NbO ₃ (ionic)	0.38	_	Ce _{1/3} TaO ₃ (ionic)	0.44	_
Ce _{1/3} NbO ₃ (electronic/total)	0.40		Ce _{1/3} TaO ₃ (electronic/total)	0.42	
			Gd _{1/3} TaO ₃ (total)<	-	0.82

largest for the most conductive samples (lanthanum-based). This is not really surprising as among lanthanides, lanthanum compounds often provide the best conductance [22,23]. For the mixed ionic-electronic conductors $Ce_{1/3}NbO_3$ and $Ce_{1/3}TaO_3$, even though the ionic contribution could not be extracted from the impedance spectra at higher temperatures (>600 K), the total conductivity activation energy does not exhibit significant changes.

The activation energy values suggest a hypothesis concerning the mobile carriers. In electrolytes, an activation energy value of around 0.5 eV is consistent with bulk cationic mobile carriers (like the rare earth). So, large ions, namely La³⁺, Pr³⁺, and Nd^{3+,} are the charge carriers in these very defective perovskites. This hypothesis is consistent with previous electrical studies on these compounds [29,31], highlighting the existence of cationic conduction by a voluminous mobile carrier (La³⁺) in the $Ln_{0.33}$ NbO₃ perovskites with an activation energy (0.37 eV) close to the one obtained here (around 0.4 eV). Nevertheless, all the ionic conductivity values obtained with our niobates and tantalates are very low (<10⁻⁵ S m⁻¹ at 300 K).

Having large mobile ions responding to an electric field while remaining rather insulating, these materials may exhibit interesting electromechanical (electrostrictive) response. In addition, the large portion of unoccupied crystallographic sites is akin to the oxygen vacancies that are held as key ingredients for the electrostrictive properties

of doped ceria [49-51].

Electrostriction properties. The maximum applied electric field for all pellets is 3 MV/m (except $Gd_{1/3}TaO_3$ where it's 5 MV/m) and the thickness is around 1.5 mm for each sample. The results of polarization and strain measurements carried out under high electric field amplitudes are presented in Fig. 12 for the niobates and in Fig. 13 for the tantalates. The electrostrictive properties depend on the rare-earth. The relative permittivities extracted from these experiments are consistent with impedance spectroscopy (i.e., under low electric field amplitude) results, confirming the independence of the permittivity on the amplitude of the electric field and the linear dielectric nature of the samples. The ions occupying the B-site of the perovskite structure have a larger influence on the electrical behaviour than those occupying the A-site. Indeed, the relative permittivity (under an electric field of 3 MV/m and at 100 Hz) of $Ln_{1/3}TaO_3$ ranges from 52 to 62, whereas it ranges from 140 to 160 for $Ln_{1/3}NbO_3$.

The electrostrictive coefficients of $Ln_{1/3}$ NbO₃ samples are below the detection limit of the setup ($M=5\times 10^{-20}~m^2/V^2$ and $Q=0.03~m^4/C^2$ with samples around 1 mm thick under an electric field of 3 MV/m). Nevertheless, when gadolinium is present in the structure, a small strain is detected, with field- and polarization-electrostrictive coefficients of $M_{33}=2\times 10^{-19}~m^2/V^2$ and $Q_{33}=0.7~m^4/C^2$ respectively. However, these values remain very low compared to those measured for the best

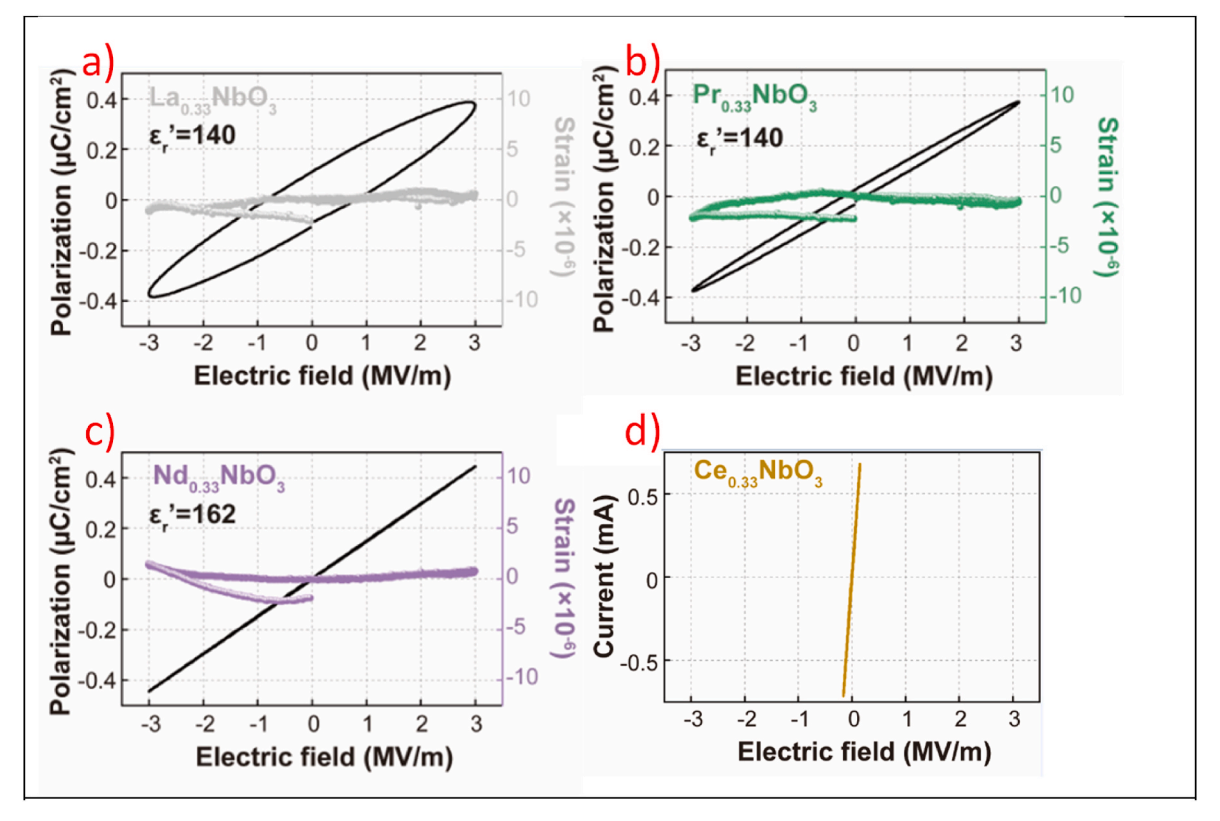


Fig. 12. Electrostriction measurement for the perovskites Ln_{0.33}NbO₃ (La_{0.33}NbO₃ (a); Pr_{0.33}NbO₃ (b); Ndr_{0.33}NbO₃ (c) and Ce_{0.33}NbO₃ (d).

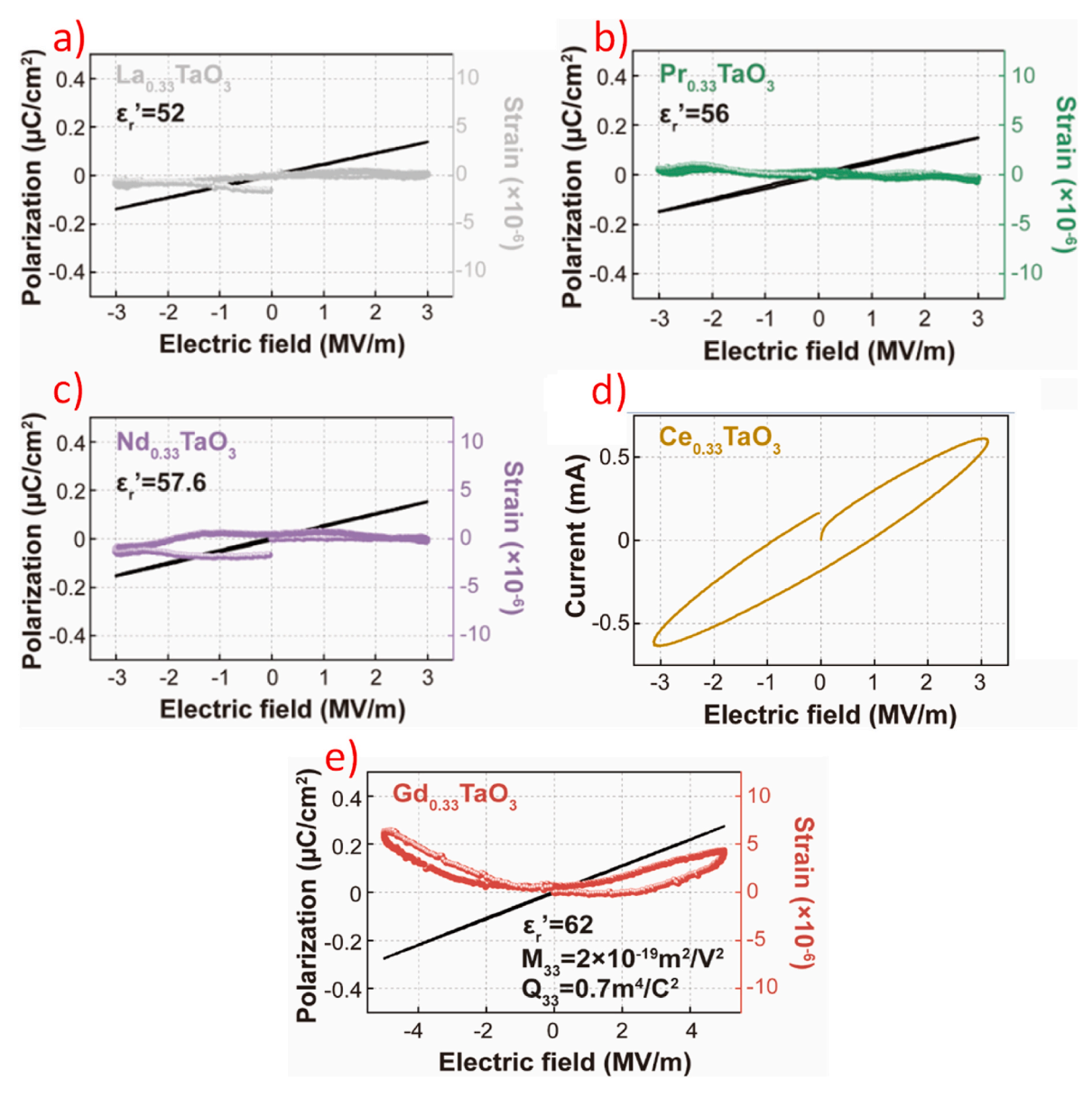


Fig. 13. Electrostriction measurement for the perovskites Ln_{0.33}TaO₃ (La_{0.33}TaO₃ (a); Pr_{0.33}TaO₃ (b); Ndr_{0.33}TaO₃ (c); Ce_{0.33}TaO₃ (d) and Gd_{0.33}TaO₃ (e).

inorganic electrostrictive materials. For instance, M is approximately $10^{-18} \,\mathrm{m^2/V^2}$ for rare-earth doped $\mathrm{CeO_2}$ ceramics [52,53], and can reach 10⁻¹⁷ m²/V² for other fluorite-type compounds such as Bi₇N $b_{0.4}Y_{1.6}O_{13.9}$ [54]. This difference is also reflected in the strain values of these ceramics: in our case, the measured strain is around 0.0005 % under an electric field of 5 MV/m ($x = M \times E^2$ [55]), whereas the strain can reach up to 0.005 % for Gd-doped LAMOX compounds (a family of materials based on La₂Mo₂O₉ [56]) under a similar electric field [57]. For the compound Gd_{1/3}TaO₃, these values are typical of "normal" rather than "giant" electrostrictors as the expected values are around 7× $10^{-20} m^2/V^2$ for M and around $0.1 m^4/C^2$ for Q (these coefficients were calculated from Ref. [58] and ref. [55] with a Youngs' modulus E=179GPa [59]). These "normal" values highlight that an incomplete cationic sublattice (with a high number of vacancies) is not a structural feature required for the onset of "giant" electrostriction. On the contrary, if there is a common underlying mechanism behind this phenomenon, the presence of an excessive number of crystallographic vacancies — as found in compounds of the Ln_{1/3}BO₃ type — significantly hinders this electromechanical deformation mechanism. The fact that only the perovskite containing gadolinium presents a measurable electrostrictive

response is intriguing. Interestingly, Gd-doped ceria also demonstrates the highest electrostrictive response among doped-ceria systems [51], and Gd-containing LAMOX compounds exhibit similar enhancements [57,60]. As mentioned before, the strong distortion of the cuboctahedron may have an important effect on Gd³⁺ mobility. The electrostrictive measurement confirms the hypothesis that the narrow squared-face bottleneck prevents Gd³⁺ from jumping to another site. The confinement of its movement within its own cage may be responsible for its electrostrictive properties. The generality of this hypothesis would require the local environment of Gd in ceria and LAMOX compounds to be studied in more detail.

4. Conclusion

Two families of tantalates and niobates perovskites were synthesized with different rare earth on the A site. The structural studies conducted via X-ray diffraction showed that all these perovskites crystallize in an orthorhombic cell (with the space group *Cmmm*) except for La_{1/3}TaO₃ which crystallizes in a tetragonal cell (with the space group *P4/mmm*). The application of network reconstruction in reciprocal space using TEM

resolved the discrepancy between the previously proposed space groups. Rietveld refinements of X-ray diagrams indicated that only half of the available cuboctahedron sites host rare earth cations, with only half a crystallographic site occupied. Furthermore, based on the formula and the refinement results, it was determined that only two-thirds of this site is occupied. HRTEM analysis showed that rare earths are randomly distributed on this site, with no evidence of pseudo-periodicity. The specific study of the lanthanide environments highlighted the unique characteristics of Gd_{1/3}TaO₃, which exhibits a strong distortion of the cuboctahedron. The first comparative study using complex impedance spectroscopy between tantalates and niobates revealed that niobates generally have conductivities two orders of magnitude higher than tantalates. This behaviour can be attributed to the microstructure and local electronic exchange on the niobium site. Additionally, the first electrostriction measurements conducted on these perovskites demonstrated that the presence of a high number of vacancies on the cationic site is not a necessary condition for the onset of giant electrostriction. Only the Gd-containing tantalate exhibited a measurable electrostrictive strain due to the confinement of the Gd ion in its cuboctahedral cage. The unique behaviour of Gd in our samples is reminiscent of the superior giant electrostriction present in Gd-doped ceria and Gd-LAMOX. Thus, we can confirm that the presence of gadolinium in a structure enhances the electromechanical properties of the ceramics. Finally, the "normal" electrostrictive response of Gd_{1/3}TaO₃ suggests that in such structures, any long-range mobility may be prevented by the local environment.

CRediT authorship contribution statement

Théo Grivois: Writing – original draft, Investigation, Formal analysis, Data curation, Conceptualization. Tomas Šalkus: Writing – original draft, Formal analysis, Data curation. Jiacheng Yu: Formal analysis, Data curation. Vilma Kavaliukė: Supervision, Funding acquisition. Pierre-Eymeric Janolin: Validation, Supervision, Funding acquisition. Saulius Daugėla: Formal analysis, Data curation. François Goutenoire: Validation, Supervision. Anthony Rousseau: Validation, Investigation, Data curation. Maud Barre: Validation, Supervision, Project administration, Funding acquisition.

Author information

Corresponding Author Theo.Grivois@univ-lemans.fr.

Funding sources

This work was partially supported by the MEGAEM ANR-19-ASTR-0024, MEGAFILM ANR-20-CE08-0012 and "PHC GILIBERT" program (project number: 48899UC), funded by the French Ministry for Europe and Foreign Affairs, the French Ministry for Higher Education and Research and the Research Council of Lithuania (LMTLT) (project number S-LZ-23-4).

Declaration of competing interest

The authors declare the following financial interests/personal relationships which may be considered as potential competing interests: Pierre-Eymeric Janolin reports financial support was provided by ANR. Maud Barre reports financial support was provided by French Ministry of Europe and Foreign Affairs. Vilma Kavaliuke reports financial support was provided by Research Council of Lithuania. If there are other authors, they declare that they have no known competing financial interests or personal relationships that could have appeared to influence the work reported in this paper.

Acknowledgment

This work was partially supported by the "PHC GILIBERT" program

(project number: 48899UC), funded by the French Ministry for Europe and Foreign Affairs, the French Ministry for Higher Education and Research and the Research Council of Lithuania (LMTLT) (project number S-LZ-23-4).

The authors greatly acknowledge "Electronic Microscopy" and "Diffusion, Diffraction and Reflectivity of X-rays" Platforms of IMMM, Le Mans Université. They also are thankful to Dr. Denis Pelloquin,from CRISMAT (Caen) for working and providing HRTEM simulations.

Appendix A. Supplementary data

Supplementary data to this article can be found online at https://doi.org/10.1016/j.ceramint.2025.08.391.

References

- R.H. Mitchell, Perovskites: Modern and Ancient, Almaz Press, Thunder Bay, Ontario, 2002.
- [2] A.M. Glazer, S.A. Mabud, Powder profile refinement of lead zirconate titanate at several temperatures. II. Pure PbTiO₃, Acta Cryst. B34 (1978) 1065–1070, https:// doi.org/10.1107/S0567740878004938.
- [3] N. Ishizawa, F. Marumo, T. Kawamura, M. Kimura, Compounds with perovskitestype slabs. II. The crystal structure of Sr₂Ta₂O₇, Acta Cryst B32 (1976) 2564–2566, https://doi.org/10.1107/S0567740876008261.
- [4] J.C. Guitel, M. Marezio, J. Mareschal, Single-crystal synthesis and structural refinement of GdGaO₃, Mat. Res. Bull. 11 (1976) 11 739–744, https://doi.org/ 10.1016/0025-5408(76)90153-7.
- [5] J.M. Moreau, C. Michel, R. Gerson, W.J. James, Ferroelectric BiFeO₃ X-ray and neutron diffraction study, J. Phys. Chem. Solid. 32 (1971) 1315–1320, https://doi. org/10.1016/S0022-3697(71)80189-0.
- [6] L.G. Tejuca, J.L.G. Fierro, J.M.D. Tascon, Structure and reactivity of perovskitetype oxides, Adv. Catal. 36 (1989) 237–328, https://doi.org/10.1016/S0360-0564 (08)60019-X.
- [7] A.G. Belous, Structural aspects and ionic conductivity in perovskite like doped niobates and titanates, Ionics 3 (1997) 117–121, https://doi.org/10.1007/ RE02375533
- [8] M. Nakayama, M. Wakihara, Y. Kobayashi, H. Miyashiro, Investigation on the arrangement of lithium ions in Li_xLa_{1/3}NbO₃ with perovskite structure, J. Phys. Chem. B 109 (2005) 14648–14653, https://doi.org/10.1021/jp052142r.
- [9] T. Yan, R. Ding, D. Ying, Y. Huang, Y. Huang, C. Tan, X. Sun, P. Gao, E. Liu, An intercalation pseudocapacitance-driven perovskite NaNbO₃ anode with superior kinetics and stability for advanced lithium-based dual-ion batteries, J. Mater. Chem. A 7 (2019) 22884–22888, https://doi.org/10.1039/C9TA09233A.
- [10] O. Bohnke, C. Bohnke, J.L. Fourquet, Mechanism of ionic conduction and electrochemical intercalation of lithium into the perovskite lanthanum lithium titanate, Solid State Ion 91 (1996) 21–31, https://doi.org/10.1016/S0167-2738 (96)00434-1
- [11] Y. Zhao, J. Zhu, H. Wang, Z. Ma, L. Gao, Y. Liu, Y. Liu, Y. Shu, J. He, Enhanced optical reflectivity and electrical properties in perovskite functional ceramics by inhibiting oxygen vacancy formation, Ceram. Int. 47 (2021) 5549–5558, https://doi.org/10.1016/j.ceramint.2020.10.139.
- [12] M. Era, S. Morimoto, T. Tsutsui, S. Saito, Organic-inorganic heterostructure electroluminescent device using a layered perovskite semiconductor (C₆H₅C₂H₄NH₃)₂PbI₄, Appl. Phys. Lett. 65 (1994) 676–678, https://doi.org/ 10.1063/1.112265.
- [13] H. Cho, S.H. Jeong, M.H. Park, Y.H. Kim, C. Wolf, C.L. Lee, J.H. Heo, A. Sadhanala, N. Myoung, S. Yoo, S.H. Im, R.H. Friend, T.W. Lee, Overcoming the electroluminescence efficiency limitations of perovskite light-emitting diodes, Science 350 (2015) 1222–1225, https://doi.org/10.1126/science.aad1818.
- [14] D.J. Bell, T.J. Lu, N.A. Fleck, S.M. Spearing, MEMS actuators and sensors: observations on their performance and selection for purpose, J. Micromech. Microeng. 15 (2005) S153–S164, https://doi.org/10.1088/0960-1317/15/7/022.
- [15] T. Zheng, J. Wu, D. Xiao, J. Zhu, Recent development in lead-free perovskite piezoelectric bulk materials, Prog. Mater. Sci. 98 (2018) 552–624, https://doi.org/ 10.1016/j.pmatsci.2018.06.002.
- [16] H.P. Rooksby, E.A.D. White, S.A. Langston, Perovskite-type rare-earth niobates and tantalates, J. Am. Ceram. Soc. 48 (1965) 447–449, https://doi.org/10.1111/ illa.2016.1965. bid.4705.x
- [17] N.P. Iyer, A.J. Smith, Double oxides containing niobium, tantalum or protactinium. III. Systems involving the rare earths, Acta Cryst 23 (1967) 740–746, https://doi. org/10.1107/S0365110X67003639.
- [18] E. Ruiz Trejo, J.F. Gomez-Garcia, Defect chemistry and electrical conductivity in the Mg and Y doped-CeNb₃O₉ perovskite, ECS Trans. 15 (2008) 99–110, https://doi.org/10.1149/1.3046624.
- [19] T. Mondal, P.M. Sarun, S. Das, T.P. Sinha, Investigation of dielectric properties of La_{0.33}NbO₃ ceramics, AIP Conf. Proc. 1665 (2015) 110043, https://doi.org/ 10.1063/1.4918099.
- [20] G. Adachi, N. Imanaka, Rare earth contribution in solid state electrolytes, especially in the chemical sensor field, J. Alloys Compd. 250 (1997) 492–500, https://doi.org/10.1016/S0925-8388(96)02628-X.

- [21] N. Imanaka, G. Adachi, Rare earth ion conduction in tungstate and phosphate ions, J. Alloys Compd. 344 (2002) 137–140, https://doi.org/10.1016/S0925-8388(02) 00352-3
- [22] M. Barré, F. Le Berre, M.P. Crosnier-Lopez, O. Bohnké, J. Emery, J.L. Fourquet, La³ + diffusion in the NASICON-type compound La_{1/3}Zr₂(PO₄)₃: X-ray thermodiffraction, ³¹P NMR, and ionic conductivity investigations, Chem. Mater. 18 (2006) 5486–5491, https://doi.org/10.1021/cm061610m.
- [23] F. Tietz, F. Urland, Lanthanide ion exchange in sodium-β-alumina, Solid State Ion 46 (1991) 331–335, https://doi.org/10.1016/0167-2738(91)90234-3.
- [24] S. Ebisu, H. Morita, S. Nagata, Influence of cubic crystal field on the magnetic susceptibility of defect-perovskite RTa₃O₉ (R= rare earth), J. Phys. Chem. Solid. 61 (2000) 45–65, https://doi.org/10.1016/S0022-3697(99)00227-9.
- [25] Q. Zhou, P.J. Saines, N. Sharma, J. Ting, B.J. Kennedy, Crystal structures and phase transitions in A-site deficient perovskites Ln_{1/3}TaO₃, Chem. Mater. 20 (2008) 6666–6676, https://doi.org/10.1021/cm8014868.
- [26] A.M. Abakumov, R.V. Shpanchenko, E.V. Antipov, Synthesis and properties of niobium bronzes R_{1+x}Nb₃O₉ (R=La,Ce,Nd), Mater. Res. Bull. 30 (1995) 97–103, https://doi.org/10.1016/0025-5408(94)00100-6.
- [27] Z. Zhang, C.J. Howard, B.J. Kennedy, K.S. Knight, Q. Zhou, Crystal structure of Ln0.33NbO3 (Ln=Nd, Pr) and phase transition in Nd_{1/3}NbO₃, J. Solid State Chem. 180 (2007) 1846–1851, https://doi.org/10.1016/j.jssc.2007.03.029.
- [28] L. Carrillo, M.E. Villafuerte-Castrejon, G. Gonzalez, L.E. Sansores, L. Bucio, J. Duque, R. Pomes, Superstructure determination of the perovskite β-La₀₋₃₃NbO₃, J. Mater. Sci. 35 (2000) 3047–3052, https://doi.org/10.1023/A:1004863715548.
- [29] A.M. George, A.N. Virkar, Mixed iono-electronic conduction in β-LaNb₃O₉, J. Phys. Chem. Solid. 49 (1988) 743–751, https://doi.org/10.1016/0022-3697(88)90023-6
- [30] A.P. Pivovarova, V.I. Strakhov, V.P. Popov, P.A. Tikhonov, Electrical conduction of lanthanum metaniobate, Refract. Ind. Ceram. 43 (2002) 43–44, https://doi.org/ 10.1023/A:1015859716018.
- [31] I. Animitsa, A. Iakovleva, K. Belova, Electrical properties and water incorporation in A-site deficient perovskite La_{1-x}Ba_xNb₃O_{9-0.5x}, J. Solid State Chem. 238 (2016) 156–161, https://doi.org/10.1016/j.issc.2016.03.023.
- [32] T. Degen, M. Sadki, E. Bron, U. Konig, G. Nénert, The Highscore suite, Powder Diffr. 29 (2014) S13–S18.
- [33] V. Petricek, L. Palatinus, J. Plasil, M. Dusek, JANA 2020- a new version of the crystallographic computing system JANA, Z. Kristallogr. 238 (2023) 271–282, https://doi.org/10.1515/zkri-2023-0005.
- [34] A. Kežionis, P. Butvilas, T. Šalkus, S. Kazlauskas, D. Petrulionis, T. Žukauskas, E. Kazakevičius, A.F. Orliukas, Four-electrode impedance spectrometer for investigation of solid ion conductors, Rev. Sci. Instrum. 84 (2013) 013902, https:// doi.org/10.1063/1.4774391.
- [35] A.M. Glazer, The classification of tilted octahedra in perovskites, Acta Cryst. B 28 (1972) 3384–3392, https://doi.org/10.1107/S0567740872007976.
- [36] Y. Inaguma, T. Katsumata, M. Itoh, Y. Morii, T. Tsurui, Structural investigations of migration pathways in lithium ion-conducting La_{2/3-x}Li_{3x}TiO₃ perovskites, Solid State Ion 177 (2006) 3037–3044. https://doi.org/10.1016/j.ssi.2006.08.012.
- [37] D. Kepaptsoglou, J.D. Baran, F. Azough, D. Ekren, D. Srivastava, M. Molinari, S. C. Parker, Q.M. Ramasse, R. Freer, Prospects for engineering thermoelectric properties in La_{1/3}NbO₃ ceramics revealed via atomic-level characterization and modeling, Inorg. Chem. 57 (2018) 45–55, https://doi.org/10.1021/acs.iporcchem/P01584
- [38] B.J. Kennedy, C.J. Howard, Phase transition behaviour in the A-site deficient perovskite oxide La_{1/3}NbO₃, J. Solid State Chem. 177 (2004) 4552–4556, https://doi.org/10.1016/j.jssc.2004.08.047.
- [39] P. Lightfoot, D.A. Woodcock, J.D. Jorgensen, S. Short, Low thermal expansion materials: a comparison of the structural behaviour of La_{0.33}Ti₂(PO₄)₃, Sr_{0.5}Ti₂(PO₄)₃ and NaTi₂(PO₄)₃, Int. J. Inorg. Mater. 1 (1999) 53–60, https://doi. org/10.1016/S1463-0176(99)00008-3.
- [40] M. Barre, M.P. Crosnier-Lopez, F. Le Berre, J. Emery, E. Suard, J.-L. Fourquet, Room temperature crystal structure of La_{1/2}Zr₂(PO₄)₃, a NASICON-type compound, Chem. Mater. 17 (2005) 6605–6610, https://doi.org/10.1021/ cm0515045.
- [41] N. Ishizawa, F. Marumo, T. Kawamura, M. Kimura, The crystal structure of Sr₂Nb₂O₇, a compound with perovskite-type slabs, Acta Crystallogr. Sect. B 31 (1975) 1912–1915, https://doi.org/10.1107/S0567740875006462.

- [42] M. Mann, S. Jackson, J. Kolis, Hydrothermal crystal growth of the potassium niobate and potassium tantalate family of crystals, J. Solid State Chem. 183 (2010) 2675–2680, https://doi.org/10.1016/j.jssc.2010.09.011.
- [43] C.J. Howard, H.T. Stokes, Octahedral tilting in cation-ordered perovskites a group-theoretical analysis, Acta Crystallogr. Sect. B 60 (2004) 674–684, https://doi.org/10.1107/S0108768104019901.
- [44] M. Klinger, More features, more tools, more CrysTBox, J. Appl. Cryst. 50 (2017) 1226-1234, https://doi.org/10.1107/S1600576717006793.
- [45] S. Roudeau, F. Weill, S. Pechev, J.M. Bassat, J.C. Grenier, Electron microscopy and structural studies of Nd_{1/3}NbO₃, C. R. Chimie 11 (2008) 734–740, https://doi.org/ 10.1016/j.crci.2007.10.002.
- [46] A. Kežionis, T. Šalkus, M. Dudek, D. Madej, M. Mosiałek, B.D. Napruszewska, W. Łasocha, M.B. Hanif, M. Motola, Investigation of alumina- and scandia-doped zirconia electrolyte for solid oxide fuel cell applications: insights from broadband impedance spectroscopy and distribution of relaxation times analysis, J. Power Sources 591 (2024) 1–11, https://doi.org/10.1016/j.jpowsour.2023.23846.
- [47] J.E. Bauerle, Study of solid electrolyte polarization by a complex admittance method, J. Phys. Chem. Solid. 30 (1969) 2657–2670, https://doi.org/10.1016/ 0022-3697(69)90039-0.
- [48] J. Zamudio-García, J.M. Porras-Vázquez, A. Cabeza, J. Canales-Vázquez, E. R. Losilla, D. Marrero-López, Influence of rare-earth doping content and type on phase transformation and transport properties in highly doped CeO₂, ACS Appl. Mater. Interfaces 16 (2024) 42198–42209, https://doi.org/10.1021/acsami.407437.
- [49] N. Yavo, O. Yeheskel, E. Wachtel, D. Ehre, A.I. Frenkel, I. Lubomirsky, Relaxation and saturation of electrostriction in 10 mol% Gd-doped ceria ceramics, Acta Mater. 144 (2018) 411–418, https://doi.org/10.1016/j.actamat.2017.10.056.
- [50] A. Kossoy, A.I. Frenkel, Q. Wang, E. Wachtel, I. Lubomirsky, Local structure and strain-induced distortion in Ce_{0.8}Gd_{0.2}O_{1.9}, Adv. Mater. 22 (2010) 1659–1662, https://doi.org/10.1002/adma.200902041.
- [51] R. Korobko, A. Patlolla, A. Kossoy, E. Watchel, H.L. Tuller, A.I. Frenkel, I. Lubomirsky, Giant electrostriction in Gd-doped ceria, Adv. Mater. 24 (2012) 5857–5861, https://doi.org/10.1002/adma.201202270.
- [52] R. Korobko, A. Lerner, Y. Li, E. Wachtel, A.I. Frenkel, I. Lubomirsky, In-situ extended X-ray absorption fine structure study of electrostriction in Gd doped ceria, Appl. Phys. Lett. 106 (2015) 042904, https://doi.org/10.1063/1.4906857.
- [53] A. Kabir, V.B. Tinti, M. Varenik, I. Lubomirsky, V. Esposito, Electromechanical dopant-defect interaction in acceptor-doped ceria, Mater. Adv. 1 (2020) 2717–2720, https://doi.org/10.1039/D0MA00563K.
- [54] N. Yavo, A.D. Smith, O. Yeheskel, S. Cohen, R. Korobko, E. Wachtel, P.R. Slater, I. Lubomirsky, Large nonclassical electrostriction in (Y, Nb)-stabilized δ-Bi₂O₃, Adv. Funct. Mater. 26 (2016) 1138–1142, https://doi.org/10.1002/ adfm.201503942.
- [55] R.E. Newnham, V. Sundar, R. Yimnirun, J. Su, Zhang, Q. M, Electrostriction: nonlinear electromechanical coupling in solid dielectrics, J. Phys. Chem. B 101 (1997) 10141–10150. https://doi.org/10.1021/jp971522c.
- [56] F. Goutenoire, O. Isnard, E. Suard, O. Bohnke, Y. Laligant, R. Retoux, P. Lacorre, Structural and transport characteristics of the LAMOX family of fast oxide-ion conductors, based on lanthanum molybdenum oxide La₂Mo₂O₉, J. Mater. Chem. 11 (2001) 119–124, https://doi.org/10.1039/B002962I.
- [57] J. Yu, A. Zaki, K. Mache, L. Féger, O. Ibder, S. Coste, M. Barré, P. Lacorre, P.-E. Janolin, Giant electrostriction enhanced by substitutions in La₂Mo₂O₉ anionic conductors, Adv. Funct. Mater. (2025) 250082, https://doi.org/10.1002/ adfm.202500821.
- [58] J. Yu, P.-E. Janolin, Defining "giant" electrostriction, J. Appl. Phys. 131 (2022) 170701, https://doi.org/10.1063/5.0079510.
- [59] T. Ogawa, T. Matsudaira, D. Yokoe, E. Kawai, N. Kawashima, C.A.J. Fisher, Y. Habu, T. Kato, S. Kitaoka, Spontaneously formed nanostructures in double perovskite rare-earth tantalates for thermal barrier coatings, Acta Mater. 216 (2021) 117152, https://doi.org/10.1016/j.actamat.2021.117152.
- [60] J. Yu, A. Zaki, K. Mache, O. Ibder, S. Coste, M. Barre, P. Lacorre, P.-E. Janolin, Origin of the apparent electric-field dependence of electrostrictive coefficients, Adv. Mater. Technol. 9 (2024) 2400066, https://doi.org/10.1002/ admt.202400066.